# Three-dimensional numerical simulation of $M_2$ internal tides in the East China Sea

Yoshihiro Niwa and Toshiyuki Hibiya
Department of Earth and Planetary Science, Graduate School of Science, University of Tokyo, Tokyo, Japan

Received 17 April 2003; revised 20 December 2003; accepted 29 January 2004; published 27 April 2004.

[1] The East China Sea and adjacent seas are one of the most significant generation regions of the $M_2$ internal tide in the world's oceans. In the present study, we investigate the distribution and energetics of the $M_2$ internal tide around the continental shelf edge in the East China Sea using a three-dimensional numerical model. The numerical experiment shows that $M_2$ internal tides are effectively generated over prominent topographic features such as the subsurface ridges in the Bashi/Luzon and Tokara Straits, the ridges along the Ryukyu Island chain, and the continental shelf slope in the East China Sea, the former particularly so. All of these topographic features are characterized by steep slopes at the depth of the thermocline onto which the $M_2$ barotropic tide is almost normally incident. The $M_2$ internal tides propagating away from these multiple source regions interfere with each other to create a complicated wave pattern. It is found that the calculated pattern of the $M_2$ internal tide agrees well with TOPEX/Poseidon altimeter observations. The conversion rate from $M_2$ barotropic to baroclinic energy over the whole analyzed model domain is estimated to be 35 GW. Roughly 10% of the energy in the $M_2$ surface tide incident on the prominent topographic features is converted to the $M_2$ internal tide, although about half of the $M_2$ internal tidal energy is subject to local dissipation in close proximity to the generation sites. *INDEX TERMS:* 4544 Oceanography: Physical: Internal and inertial waves; 4568 Oceanography: Physical: Turbulence, diffusion, and mixing processes; 4560 Oceanography: Physical: Surface waves and tides (1255); *KEYWORDS:* internal tide, East China Sea

**Citation:** Niwa, Y., and T. Hibiya (2004), Three-dimensional numerical simulation of $M_2$ internal tides in the East China Sea, *J. Geophys. Res.*, *109*, C04027, doi:10.1029/2003JC001923.

## 1. Introduction

[2] Internal (baroclinic) tides are ubiquitous in a stratified ocean where they are generated in response to tidal flows incident upon bottom topography such as the continental shelf slope, subsurface ridges, and seamounts. In contrast to surface tides, internal tides have a large amplitude vertical displacement of isopycnals accompanied by depth-varying currents, and are characterized by relatively short horizontal wavelengths of the order of 100 km in the open ocean. Recent analysis of TOPEX/Poseidon altimeter data has shown that energetic, low-vertical-mode internal tides can propagate more than 1000 km from their generation sites [*Ray and Mitchum*, 1996; *Ray and Cartwright*, 1998].

[3] It is widely recognized that internal tides play a significant role in large-scale oceanographic contexts. Generation of internal tides can be an important sink of the surface tidal energy [*Munk*, 1997]. Thus an accurate estimate of the conversion of the barotropic tidal energy to internal tides is essential to close the global tidal energy budget as well as the solar and lunar system evolution. Internal tides also have strong influence on the global thermohaline circulation, because they contribute significantly to deep ocean mixing [*Munk and Wunsch*, 1998]. Internal tides generated by strong tide-topography interactions occasionally break, causing intense turbulent mixing [*Polzin et al.*, 1997; *Ledwell et al.*, 2000; *Lien and Gregg*, 2001]. Turbulent mixing may also be induced far from wave generation sites, because propagating internal tides can nonlinearly interact with the background internal waves and cascade part of their energy down to small scales where breaking can occur. Recent studies suggest that the energy conversion rate of barotropic tidal energy to internal tides in the global ocean amounts to about 1 Terawatt (TW) (1 TW = $10^{12}$ W), which is about half of the energy required to maintain the global thermohaline circulation [*Munk and Wunsch*, 1998; *Egbert and Ray*, 2000; *Jayne and St. Laurent*, 2001; *Niwa and Hibiya*, 2001]. *Hasumi and Suginohara* [1999] have demonstrated with numerical simulations the sensitivity of the global thermohaline circulation to the spatial distribution of enhanced vertical diffusivity which was assumed to coincide with the distribution of rough bathymetry.

[4] As a first step toward numerical modeling of the global internal tide, *Niwa and Hibiya* [2001] examined the distribution of the $M_2$ internal tide throughout the Pacific Ocean using a full three-dimensional primitive equation model. They showed that the internal tidal energy in the western Pacific was 2–3 orders of magnitude higher


0148-0227/04/2003JC001923$09.00

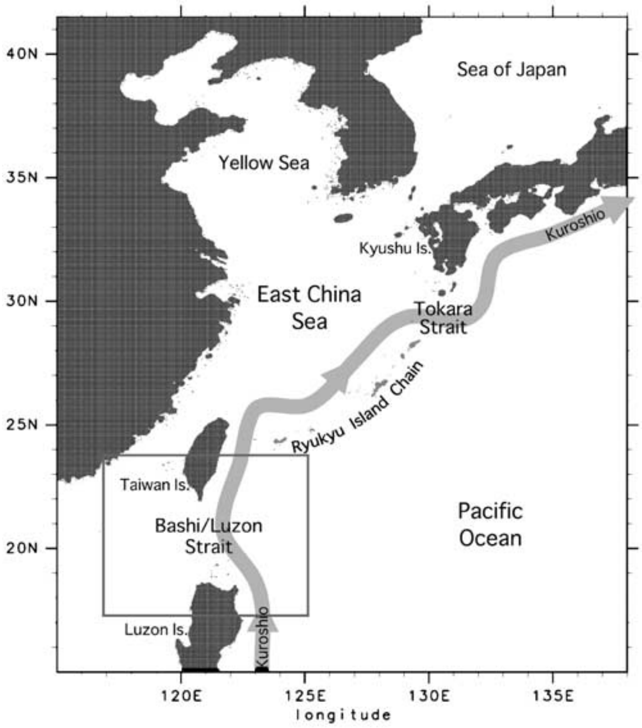


**Figure 1.** Model domain including the East China Sea and adjacent seas. The areas cited in the text are shown. The thick curve shows the typical main path of the Kuroshio. The box shows the area where the sensitivity studies of the internal tide simulation to various parameters was conducted (see Appendix A).

than in the eastern Pacific, manifesting the spatial distribution of prominent topographic features.

[5] In the western Pacific, the East China Sea and adjacent seas are one of the most important generation regions of internal tides. The area is characterized by strong barotropic tidal currents [*Kang et al.*, 1998; *Lefévre et al.*, 2000] as well as prominent topographic features in the Ryukyu Island chain and the Bashi/Luzon Strait. Nearly 10% of the estimated 340 Gigawatts (GW) (1 GW = $10^9$ W) of $M_2$ barotropic to baroclinic energy conversion integrated over the whole Pacific Ocean occurs there [*Niwa and Hibiya*, 2001]. Indeed, using a two-dimensional analytical model, *Baines* [1982] predicted that the continental shelf slope in the East China Sea is the second largest generator of the $M_2$ internal tide among the major continental shelf slopes in the world's oceans. Vigorous mixing, the strength of which depends on the phase of the semidiurnal tidal current, has been observed in the East China Sea [*Matsuno et al.*, 1994, 1997]. Evidence of strong internal wave generation is provided by synthetic aperture radar (SAR) images covering the continental shelf of the East China Sea, which show that the generated internal tides evolve into internal solitary waves while propagating shoreward from the shelf break [*Hsu et al.*, 2000].

[6] The East China Sea and adjacent seas are thus interesting regions for the study of internal tides. Nevertheless, all of the previous numerical studies of this region were concerned only with the surface tidal responses [e.g., *Kang et al.*, 1998, *Lefévre et al.*, 2000; *Matsumoto et al.*, 2000]. In the present study, we numerically investigate the spatial distribution of the $M_2$ internal tide and its energetics in the East China Sea and adjacent seas using a high-resolution, three-dimensional model that takes into account realistic tidal forcing as well as realistic bathymetry.

## 2. Numerical Model

[7] Figure 1 shows the model domain covering a longitudinal range from 115°E to 138°E and a latitudinal range from 15°N to 41.5°N. The bathymetry in the East China Sea and adjacent seas is shown in Figure 2. The major features include a prominent ridge running from the south of Kyushu Island through the Ryukyu Island chain and across the Bashi/Luzon Strait to Luzon Island, and the continental shelf slope in the East China Sea that runs parallel to this ridge. In the present study, all the topographic features north of 35°N, including the steep topographic slopes at the entrance to the Sea of Japan, are found to contribute no more than 3% of the baroclinic tidal energy conversion integrated over the whole model domain. For this reason, only the results south of 35°N are presented.

[8] The numerical simulation was carried out using the Princeton Ocean Model [*Blumberg and Mellor*, 1987], which solves the three-dimensional, free-surface primitive equations under the hydrostatic and Boussinesq approximations. The model uses a terrain-following, sigma coordinate defined by $\sigma = \frac{z-\eta}{D}$ with $z$ a vertical Cartesian coordinate positive upward, and $D$ the total water depth ($D \equiv H + \eta$ where $H$ is the time-mean water depth and $\eta$ the perturbation sea surface elevation). The sigma coordinate thus ranges from $\sigma = 0$ at the surface down to $\sigma = -1$ at the bottom. The governing equations are then given by

$$\frac{\partial UD}{\partial t}+\frac{\partial UUD}{\partial x}+\frac{\partial UVD}{\partial y}+\frac{\partial U\omega}{\partial \sigma}=+fVD-\frac{D}{\bar{\rho}_0}\frac{\partial P'}{\partial x}+\frac{\sigma}{\bar{\rho}_0}\frac{\partial P'}{\partial \sigma}\frac{\partial D}{\partial x} -\alpha g D\frac{\partial \eta}{\partial x}+\beta g D\frac{\partial \xi}{\partial x}-r\left(U-\overline{U}\right)D+F_U, \tag{1}$$

$$\frac{\partial VD}{\partial t}+\frac{\partial VUD}{\partial x}+\frac{\partial VVD}{\partial y}+\frac{\partial V\omega}{\partial \sigma}=-fUD-\frac{D}{\bar{\rho}_0}\frac{\partial P'}{\partial y}+\frac{\sigma}{\bar{\rho}_0}\frac{\partial P'}{\partial \sigma}\frac{\partial D}{\partial y} -\alpha g D\frac{\partial \eta}{\partial y}+\beta g D\frac{\partial \xi}{\partial y}-r\left(V-\overline{V}\right)D+F_V, \tag{2}$$

$$\frac{\partial P'}{\partial \sigma}=-gD(\rho-\rho_0), \tag{3}$$

$$\frac{\partial UD}{\partial x}+\frac{\partial VD}{\partial y}+\frac{\partial \omega}{\partial \sigma}+\frac{\partial \eta}{\partial t}=0, \tag{4}$$

$$\frac{\partial TD}{\partial t}+\frac{\partial TUD}{\partial x}+\frac{\partial TVD}{\partial y}+\frac{\partial T\omega}{\partial \sigma}=F_T, \tag{5}$$

$$\frac{\partial SD}{\partial t}+\frac{\partial SUD}{\partial x}+\frac{\partial SVD}{\partial y}+\frac{\partial S\omega}{\partial \sigma}=F_S, \tag{6}$$

where $t$ is time, $x$ and $y$ are defined positive eastward and northward, $U$ and $V$ are the velocity components in the $x$ and

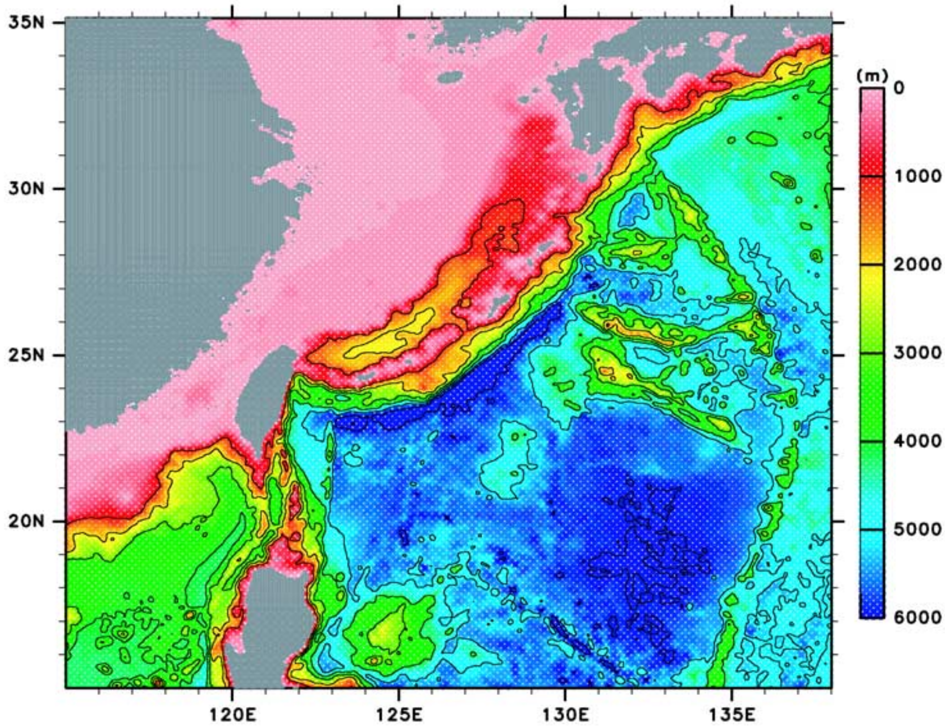


**Figure 2.** Bathymetry in the analyzed model domain.

$y$ directions, $\omega$ is the velocity component normal to the $\sigma$ = constant surfaces, $\overline{U}$ and $\overline{V}$ are the depth-averaged components of $U$ and $V$, $f = 2\Omega \sin\phi$ is the Coriolis frequency with $\Omega$ the angular velocity of the Earth's rotation and $\phi$ the latitude, $T$ and $S$ are the potential temperature and salinity, $\rho$ is the water density determined from $T$ and $S$ using the equation of state, $\rho_0$ is the background basic density stratification, $\overline{\rho}_0$ is the reference water density, $P'$ is the pressure perturbation associated with the density deviation from the background stratification, $g$ is the acceleration due to gravity, the factor $\alpha$ accounts for the effect of load tides and is assumed to be 0.9 following *Ray* [2001], $\xi$ is the equilibrium tidal potential; the factor $\beta$ multiplying $\xi$ is the effective Earth elasticity assumed to be 0.69 following *Kantha* [1995], and ($F_U$, $F_V$) and ($F_T$, $F_S$) represent the viscosity and diffusivity terms. Horizontal eddy viscosity and diffusivity coefficients were determined following the formulation of *Smagorinsky* [1963], whereas vertical eddy viscosity and diffusivity coefficients were determined using the level-2.5 turbulent kinetic energy closure model of *Mellor and Yamada* [1982]. At the lowest sigma level, bottom friction was applied through a quadratic friction law with the constant drag coefficient assumed to be 0.0025. Artificial linear damping terms were introduced to represent the decay of internal tides during the course of propagation caused by nonlinear interactions with the background internal waves; the damping coefficient $r$ was assumed to be 1/5 (days$^{-1}$) based on the estimates from previous field observations [*Munk*, 1997] as well as the resonant interaction theory [*McComas and Müller*, 1981].

[9] The model's horizontal grid spacing was 1/32° both in the longitudinal and latitudinal directions. In the vertical direction, we used 50 sigma levels which were evenly distributed from the sea surface down to the bottom. The model topography was constructed by averaging the bathymetric data of *Smith and Sandwell* [1997] within a 10 km radius at each grid point. It should be noted that this reduces the spatial resolution of the bottom topography. The sensitivity of the calculated results to this spatial averaging is examined in Appendix A, where a set of numerical experiments are reported for the localized region around the Bashi/Luzon Strait.

[10] The background basic temperature and salinity are both assumed to be horizontally homogeneous and vertically stratified. Each depth profile was obtained by horizontally averaging the annual mean data of the World Ocean Atlas [*Levitus and Boyer*, 1994; *Levitus et al.*, 1994] having water depth more than 1000 m for 120°E–135°E and 17°N–32°N. Substantial horizontal variations of temperature and salinity in the shallow waters of the East China Sea and the Yellow Sea as well as in the Kuroshio frontal zone are thus not taken into account in the present study.

[11] The present hydrostatic numerical model cannot reproduce the nonlinear evolution of internal tides into high-frequency internal waves that is frequently observed over the continental shelf [e.g., *Hsu et al.*, 2000]. Hereafter we restrict our attention to the distribution and energetics of the most dominant $M_2$ tidal constituent. The model was forced at the open boundary by prescribing the $M_2$ surface tide through a forced gravity wave radiation condition as employed by *Niwa and Hibiya* [2001]. The amplitude of the $M_2$ surface tide at the open boundary was specified by using the predictions of the global tide model of *Matsumoto et al.* [2000]. For the internal tide, a 1° wide sponge layer was assumed along each open boundary to avoid artificial reflection. Taking account of the fact that the first vertical mode internal tide takes about 10 days to propagate across the calculation domain, the model was driven for 15 days

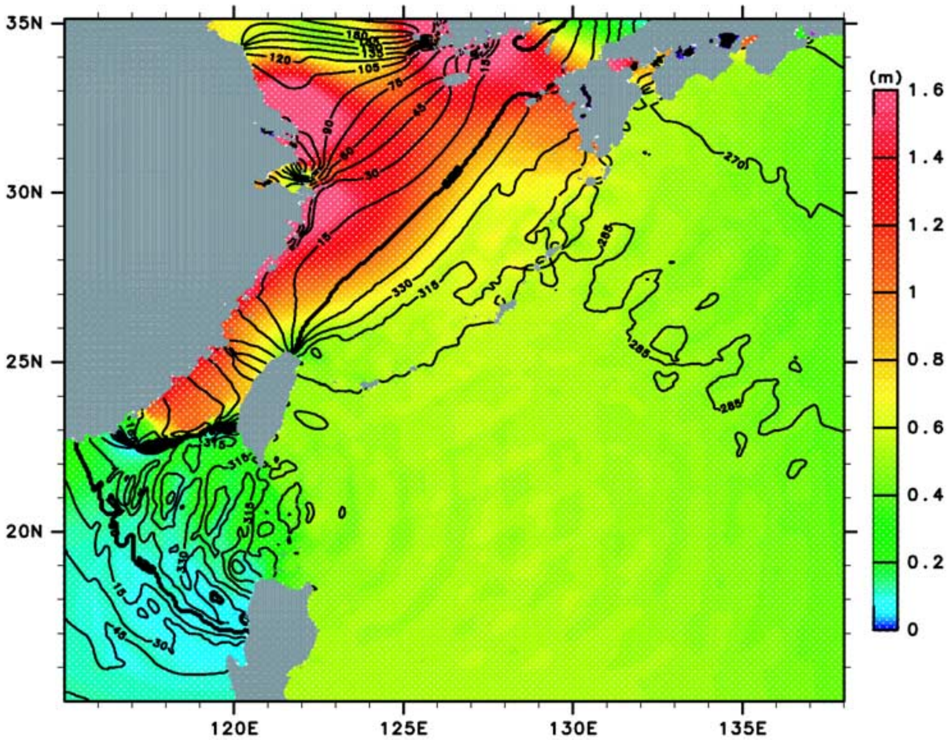


**Figure 3.** Amplitude and phase of the calculated surface elevation of the $M_2$ tide. The amplitude is denoted by color shading whereas the phase is denoted by the black contours at intervals of 15°.

from an initial state of rest with time steps of 90 s and 3 s for the baroclinic and barotropic tides, respectively. The calculated time series for the final 2 days were harmonically analyzed to obtain the amplitude and phase of the surface and internal tidal responses.

[12] It should be noted that the Kuroshio having surface current speeds of 0.75–1.5 m $s^{-1}$ and typical width of 100 km is not represented in our model. The thicker curve in Figure 1 shows the typical main path of the Kuroshio running northward along the eastern coast of Luzon and Taiwan Islands and then northwestward along the continental shelf edge of the East China Sea up to the Tokara Strait. The detailed discussions of the effects of the Kuroshio and associated density gradients on the internal tides are beyond the scope of the present study.

## 3. Results

### 3.1. $M_2$ Surface Tide Field

[13] Figure 3 shows the amplitude and phase of the calculated surface elevation in the region of concern, namely, the southern portion of the model domain (Figures 1 and 2). The calculated pattern is almost identical to those obtained previously [e.g., *Matsumoto et al.*, 2000]. In addition, sea surface signatures associated with internal tides can be detected, which will be discussed in more detail in section 3.2. The phase pattern indicates that the $M_2$ surface tide originates in the western North Pacific and propagates coastward crossing the Ryukyu Island chain and the Bashi/Luzon Strait.

[14] The validity of the calculated result is checked via a comparison with TOPEX/Poseidon altimeter observations. Figure 4 shows the RMS difference over a tidal cycle between the calculated and observed surface elevation along TOPEX/Poseidon ground tracks. We used about 5 years of TOPEX/Poseidon altimeter data to estimate the $M_2$ tidal elevation at successive points along each satellite track (for the details of the analysis of TOPEX/Poseidon altimeter data, the readers are referred to *Matsumoto et al.* [2000]). Except for the shallow coastal waters of the East China Sea where the effects of mesoscale eddies become significant, we can see overall agreement between the model predictions and TOPEX/Poseidon altimeter observations with the RMS difference being no more than 5 cm. This indicates that the tidal forcing for internal tides is reasonably well simulated by the present numerical model.

[15] Using the depth-averaged velocity ($\overline{U}$, $\overline{V}$), we can obtain the $M_2$ tidal current ellipse at each location as shown in Figure 5, where the radius of each ellipse is scaled logarithmically. Although the $M_2$ barotropic tidal currents in the western North Pacific are of the order of 0.01 m $s^{-1}$, they increase to more than 0.2 m $s^{-1}$ in the East China Sea because of shoaling effects.

### 3.2. $M_2$ Internal Tide Field

[16] The distribution of the barotropic forcing for the $M_2$ internal tide can be examined by introducing the forcing function defined by *Baines* [1982], namely,

$$F = \left(-\overline{U}\frac{\partial H}{\partial x} - \overline{V}\frac{\partial H}{\partial y}\right) \times \left(\frac{-z}{H}\right) \times \left|\frac{\partial \rho_0}{\partial z}\right|, \qquad (7)$$

where $-\frac{\partial H}{\partial x}$ and $-\frac{\partial H}{\partial y}$ are the bottom slopes in the $x$ and $y$ directions, respectively. Figure 6 shows the magnitude of

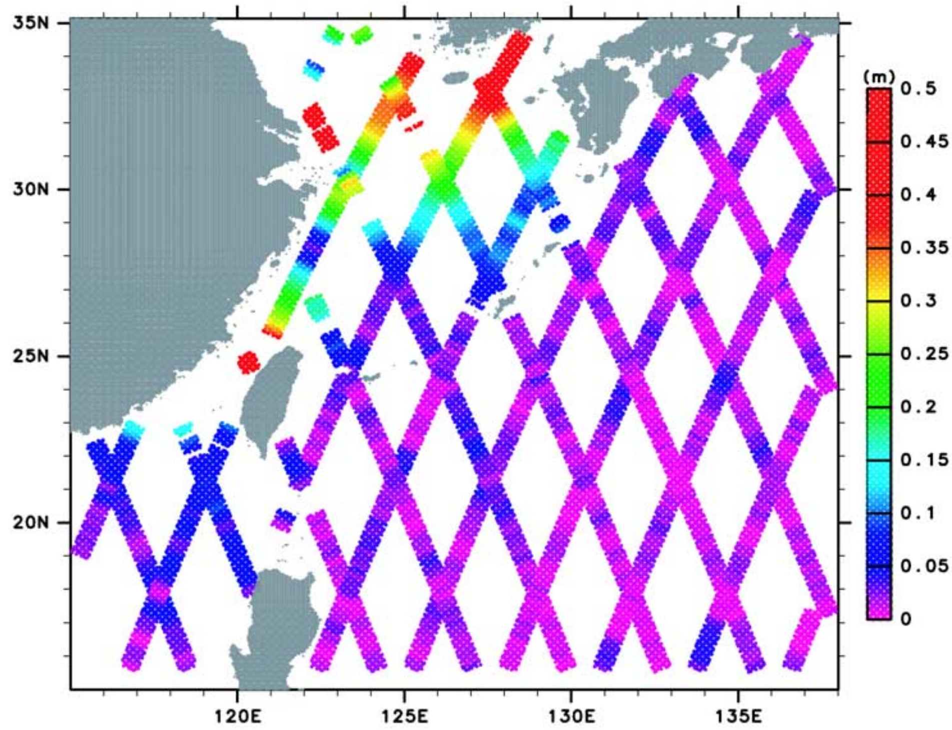


**Figure 4.** RMS difference for the surface elevation of the $M_2$ tide along TOPEX/Poseidon ground tracks between the model predictions and TOPEX/Poseidon altimeter observations.

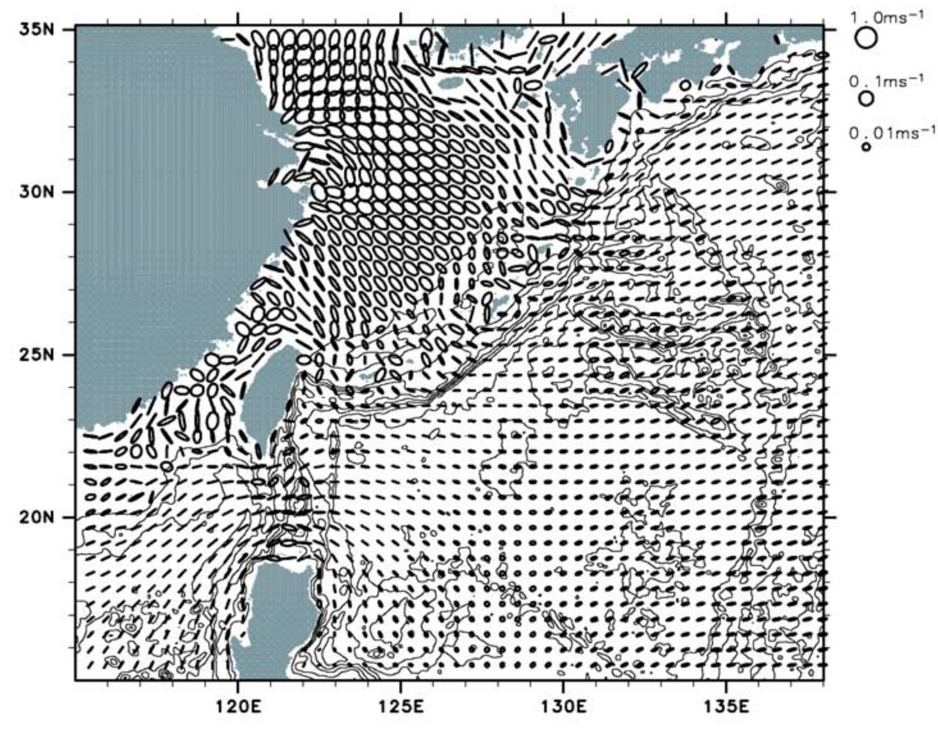


**Figure 5.** $M_2$ tidal current ellipse at each location obtained using the calculated depth-averaged horizontal velocity. The background contours show the bathymetry (contour interval is 1000 m). Note that the radius of each ellipse is scaled logarithmically.

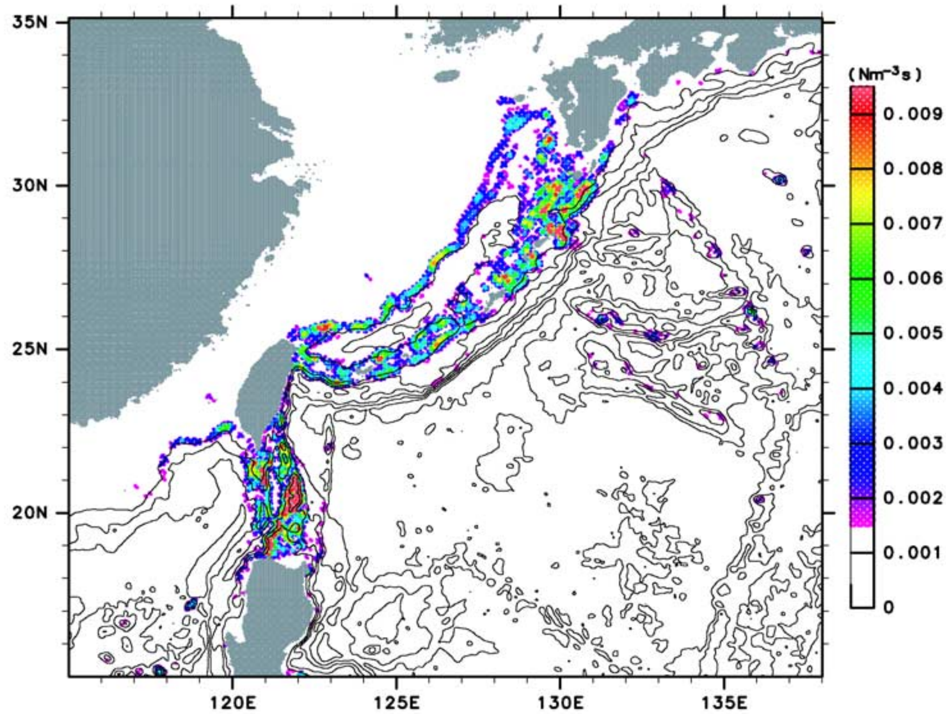


**Figure 6.** Model-predicted magnitude of the depth-integrated $M_2$ forcing function at each location averaged over the final 2 days of the calculation (for definition, see text). The background contours show the bathymetry (contour interval is 1000 m).

the depth-integrated forcing function averaged over the final 2 days of the calculation. Strong forcing occurs along the Ryukyu Island chain, especially over the continental shelf slope in the Tokara Strait south of Kyushu Island and in the Bashi/Luzon Strait where the $M_2$ surface tide is almost normally incident to prominent topographic features with steep slopes at the depth of the thermocline (see Figure 5). We can actually confirm in Figure 7 that large kinetic energy of the $M_2$ internal tide originates in the strong forcing area mentioned above.

[17] Figure 8 shows the instantaneous distributions of vertical isopycnal displacement at a depth of 1000 m at the third, fifth, ninth, and twenty-first period after the start of calculation. Figures 8a–8d indicate that although the amplitude of the $M_2$ internal tide is more than 30 m around the Ryukyu Island chain and the Bashi/Luzon Strait, it decays to about 5 m as the model boundary is approached. We can recognize the $M_2$ internal tide with a horizontal wavelength of 150–200 km propagating at a speed of 3.5–4.5 m s$^{-1}$, close to the eigenspeed of the first vertical mode. It is seen that the $M_2$ internal tides from multiple source regions such as the Bashi/Luzon Strait and the southern part of the Ryukyu Island chain interfere with each other to create a complicated wave pattern.

[18] It should be noted that the propagation speed of the $M_2$ internal tide (3.5–4.5 m s$^{-1}$) is of the same order of magnitude as the speed of the Kuroshio (0.75–1.5 m s$^{-1}$), which suggests that the spatial patterns of the $M_2$ internal tide are significantly modified by the Kuroshio in the real ocean. This advective effect is considered to be important particularly around the Tokara Strait where the propagation direction of the generated $M_2$ internal tides is nearly parallel to the Kuroshio's main path (see Figure 1). In contrast, the $M_2$ internal tides generated in the Bashi/Luzon Strait are found to cross the Kuroshio's main path almost perpendicularly, so that the advective effect is thought to be much weaker there.

[19] Next, the vertical structure of the $M_2$ internal tide is examined by taking a representative cross section along 21.5°N which transects the prominent subsurface ridges in the Bashi/Luzon Strait. Figure 9 shows the cross-sectional snapshot of vertical isopycnal displacement and horizontal velocity which are most clearly seen along a ray emanating from the top of the ridge. This ray-like structure, however, vanishes after a couple of reflections at the sea surface and bottom, suggesting that the high vertical modes are dissipated close to the generation site. Consequently, away from generation sites the first vertical mode dominates the vertical structure with the highest velocity in the upper 500 m reaching about 0.15 m s$^{-1}$ and maximum vertical isopycnal displacement found at mid-depth between 1000 and 2000 m.

[20] As mentioned earlier, the surface elevation shown in Figure 3 is affected by the underlying $M_2$ internal tides. These signals are recognized as short-wavelength (~100 km) fluctuations superposed on the co-range and co-phase lines in the western North Pacific which can be detected by TOPEX/Poseidon altimeter observations [*Matsumoto et al.*, 2000]. Figure 10 shows the short-wavelength surface elevation amplitude fluctuations along TOPEX/Poseidon ground tracks obtained from the numerical experiment (thick solid lines) and from TOPEX/Poseidon altimeter observations (thin solid lines). To extract the surface fluctuations of the $M_2$ internal tides, high-pass filtering with a cutoff wavelength of 300 km (a few times the internal tide wavelength of 150 to 200 km) was applied along each

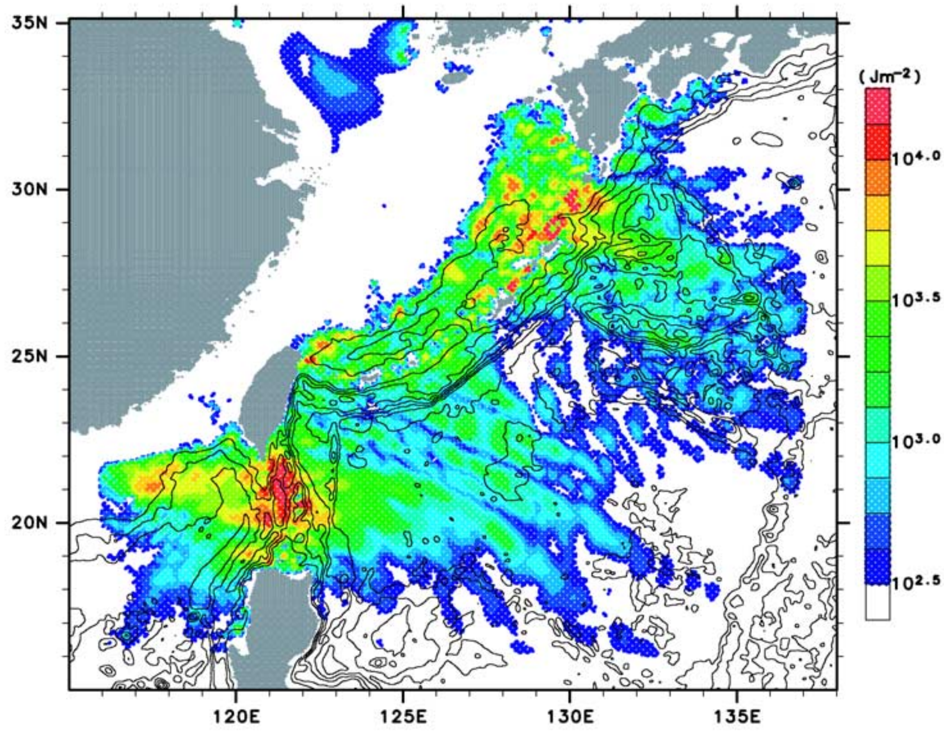


**Figure 7.** Model-predicted distribution of the depth-integrated kinetic energy of the $M_2$ internal tide averaged over the final 2 days of the calculation. The background contours show the bathymetry (contour interval is 1000 m).

TOPEX/Poseidon ground track. We can see that the magnitude and wavelength of the model predicted surface fluctuations are in general agreement with TOPEX/Poseidon altimeter observations. The agreement is better for the descending ground track (left panel) running roughly parallel to the propagation direction of the $M_2$ internal tides. Around the Tokara Strait, however, significant discrepancies are found between the model predictions and observations, possibly because the internal tides are strongly modified by the Kuroshio. Figure 11 shows the same comparison for the case where the linear damping of the $M_2$ internal tide was omitted (i.e., $r = 0$ in the governing equations (1) and (2)). In this case, the model prediction overestimates the amplitudes of the surface fluctuations in the southeastern part of the model domain (longitudes > 130°E and latitudes < 21°N), a region more than 500 km away from the major sources of the $M_2$ internal tides. This suggests that the adoption of the 5-day damping of the $M_2$ internal tide is essential for the successful numerical simulation away from wave generation sites.

### 3.3. Energetics of the $M_2$ Internal Tide

[21] The generation of the $M_2$ internal tide can be discussed more quantitatively based on the energetics. The governing equation for the depth-integrated baroclinic energy is given by

$$\frac{\partial \overline{E}_{bc}D}{\partial t} = -\left(\frac{\partial \overline{P'U'}D}{\partial x} + \frac{\partial \overline{P'V'}D}{\partial y}\right) + g\overline{\rho' w_{bt}}D + \overline{DIS}_{bc} + \overline{ADV}_{bc}, \tag{8}$$

where the primed variables are baroclinic components, the overbar denotes the average over the entire water column, $E_{bc}$ is the baroclinic energy density, $w_{bt}$ is the Cartesian vertical velocity associated with the barotropic flow given by

$$w_{bt} = \overline{U}\left(\sigma\frac{\partial D}{\partial x} + \frac{\partial \eta}{\partial x}\right) + \overline{V}\left(\sigma\frac{\partial D}{\partial y} + \frac{\partial \eta}{\partial y}\right) + (\sigma + 1)\frac{\partial \eta}{\partial t}, \tag{9}$$

and $DIS_{bc}$ and $ADV_{bc}$ denote the dissipation and advection of the baroclinic energy, respectively. The first term on the right-hand side of equation (8) is the divergence of the depth-integrated baroclinic energy flux. The second term, $g\overline{\rho' w_{bt}}D$, represents the rate of conversion from barotropic to baroclinic energy integrated over the entire water column.

[22] The governing equation for the depth-integrated barotropic energy, on the other hand, is given by

$$\begin{aligned}\frac{\partial E_{bt}D}{\partial t} = &-\left\{\frac{\partial\left(\overline{\rho}_0 g(\alpha\eta - \beta\xi) + \overline{P}'\right)\overline{U}D}{\partial x}\right. \\ &\left. + \frac{\partial\left(\overline{\rho}_0 g(\alpha\eta - \beta\xi) + \overline{P}'\right)\overline{V}D}{\partial y}\right\} - g\overline{\rho' w_{bt}}D \\ &+ \overline{\rho}_0 g((1-\alpha)\eta + \beta\xi)\frac{\partial \eta}{\partial t} + \overline{DIS}_{bt} + \overline{ADV}_{bt},\end{aligned} \tag{10}$$

where $E_{bt}$ is the barotropic energy density, and $DIS_{bt}$ and $ADV_{bt}$ denote the dissipation and advection of the barotropic energy, respectively. The first term on the right-hand side of equation (10) is the divergence of the depth-integrated barotropic energy flux, and the third term represents the work done by the tide generating force and the elastic earth.

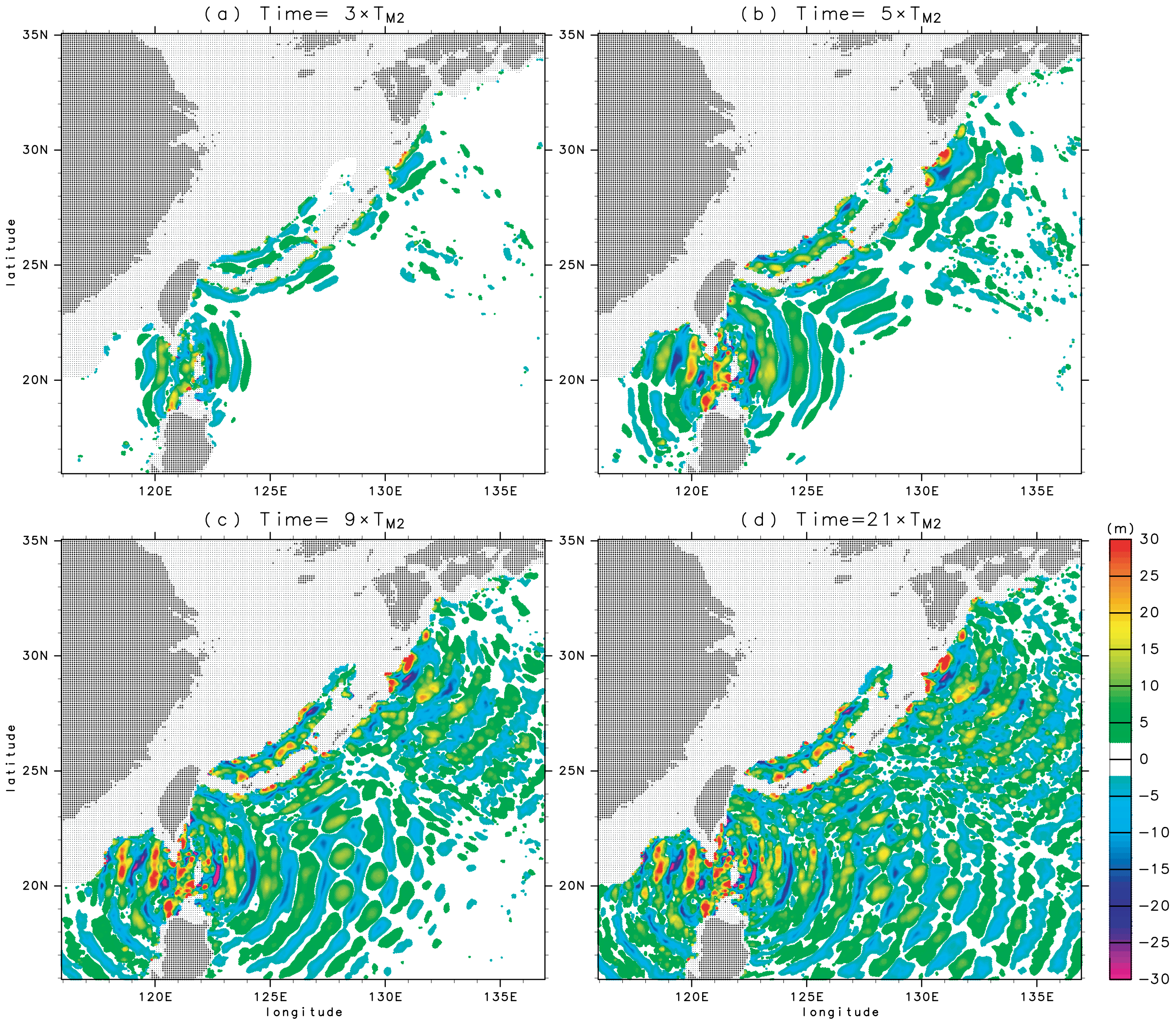


**Figure 8.** Model-predicted distribution of the vertical isopycnal displacement at a depth of 1000 m after the (a) third, (b) fifth, (c) ninth, and (d) twenty-first $M_2$ tidal period from the start of the calculation.

[23] Integrating equations (8) and (10) over a fixed area and taking an average over one tidal period (denoted by an angled bracket) yields the conservation equations for the baroclinic and barotropic energy,

$$\int_C \langle \overline{P'U_n'D} \rangle dl = \iint_S \langle g\overline{\rho' w_{bt} D} \rangle dS + \iint_S \langle \overline{DIS_{bc}} \rangle dS + \iint_S \langle \overline{ADV_{bc}} \rangle dS \tag{11}$$

$$\int_c \left\langle \left(\overline{\rho}_0 g(\alpha\eta - \beta\xi) + \overline{P}'\right) \overline{U}_n D \right\rangle dl = -\iint_S \langle g\overline{\rho' w_{bt} D} \rangle dS + \iint_S \left\langle \overline{\rho}_0 g \beta \xi \frac{\partial \eta}{\partial t} \right\rangle dS + \iint_S \langle \overline{DIS_{bt}} \rangle dS + \iint_S \langle \overline{ADV_{bt}} \rangle dS, \tag{12}$$

where $\overline{U}_n$ and $U_n'$ denote the barotropic and baroclinic velocities outward normal to the boundary of the area $C$, respectively, $dS$ is an infinitesimal element of the area ($S$), and $dl$ is an infinitesimal line element on the boundary $C$.

[24] Integrating $\langle g\overline{\rho' w_{bt} D} \rangle$ over the whole analyzed model domain (115°E–138°E, 15°N–35°N) yields about 35 GW. This value corresponds to about 5% of the global conversion rate of the $M_2$ tide estimated by *Egbert and Ray* [2000] and about 1.5% of the power required to maintain the global thermohaline circulation [*Munk and Wunsch*, 1998]. Figure 12 shows the distribution of $\langle g\overline{\rho' w_{bt} D} \rangle$ over the prominent topographic features. The largest observed $M_2$ baroclinic energy was over the subsurface ridges in the Bashi/Luzon Strait where the net baroclinic energy conversion reaches 14 GW about 40% of the baroclinic energy conversion integrated over the whole analyzed model domain. The second largest patch of $M_2$ internal tidal energy was found over the continental shelf slope in the Tokara Strait where the net baroclinic energy conversion reaches 9.3 GW. This is nearly half of the baroclinic energy conversion integrated along all of the topographic features from Kyushu Island down to Taiwan Island (19 GW). It is also found that the net baroclinic energy conversion reaches

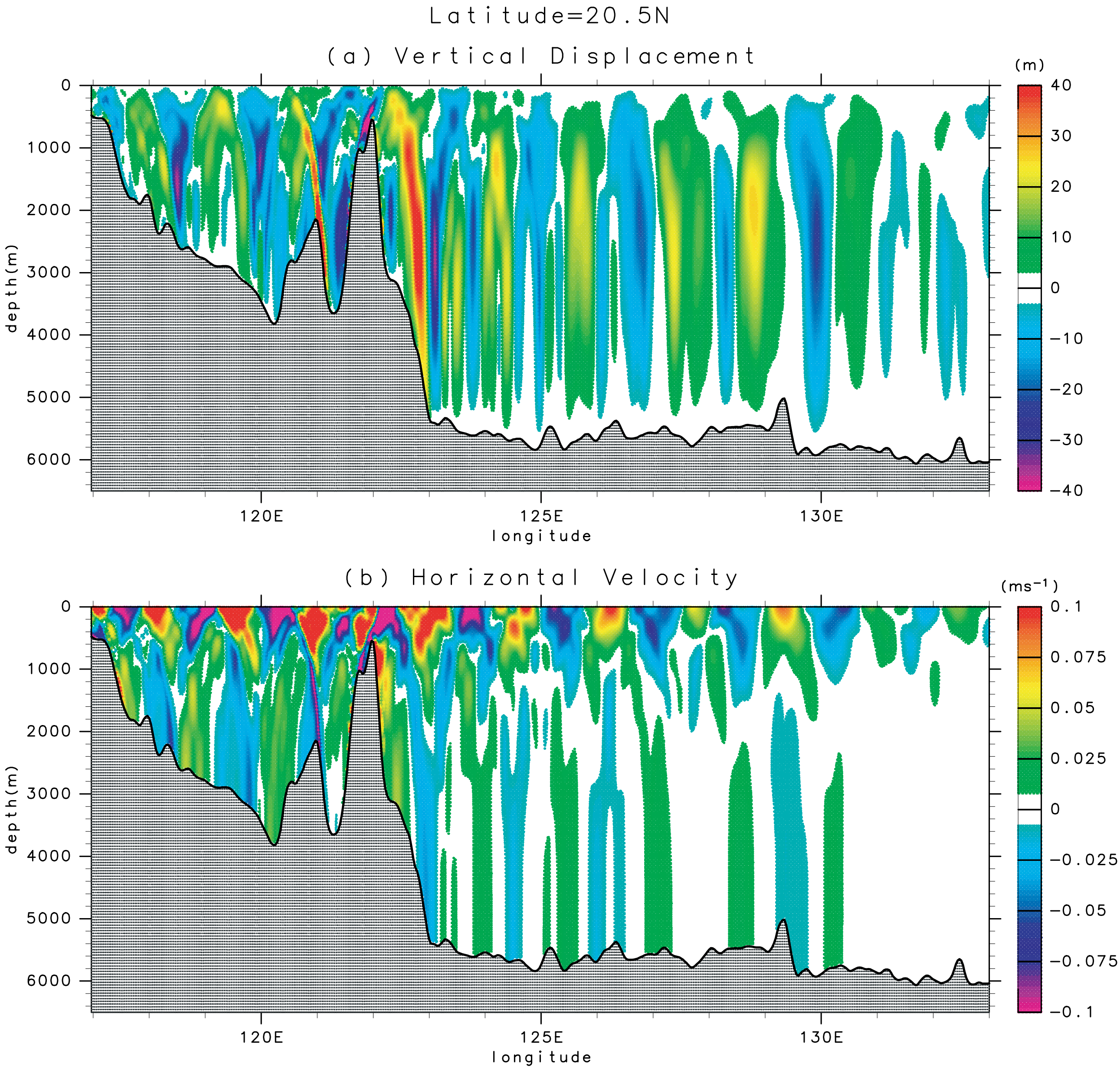


**Figure 9.** Model-predicted cross-sectional snapshot along 21.5°N of (a) vertical isopycnal displacement and (b) horizontal velocity.

4.1 GW along the continental shelf slope extending over a distance of about 1000 km. The average conversion rate at the continental slope, 4100 W m$^{-1}$, is about 3 times the previous estimate by *Baines* [1982]. The major reason for this discrepancy is thought to be attributable to the fact that three-dimensional irregularity along the bottom topography was completely ignored in Baines' analytical model. The predicted baroclinic conversion rate in our model is relatively independent of the model grid resolution, the spatial resolution of the bottom topography and the dissipation parameters (see Appendix A).

[25] The red numbers and arrows shown in Figure 12 indicate the value and direction of the $M_2$ barotropic energy flux across each section, respectively. The net $M_2$ barotropic energy flux onto the subsurface ridges in the Bashi/Luzon Strait is 56 GW, 25% of which (14 GW) is converted to $M_2$ baroclinic energy. After passing through the strait, the barotropic energy flux decreases to 41 GW, indicating 15 GW of the barotropic energy is lost within the Bashi/Luzon Strait which almost balances the conversion of barotropic to baroclinic energy. The $M_2$ barotropic energy flux incident to the prominent topographic features between Kyushu Island and Taiwan Island is 191 GW, 10% of which (19 GW) is converted to $M_2$ baroclinic energy with the residual mostly dissipated by bottom friction on the continental shelf in the East China Sea.

[26] Figure 13 shows the depth-integrated $M_2$ baroclinic energy flux where most of the excited baroclinic energy is seen to propagate seaward. This is because most of the continental shelf slope in the East China Sea is steeper than the characteristic slope of the $M_2$ internal tide so that the shoreward propagation of the excited internal tide is strongly

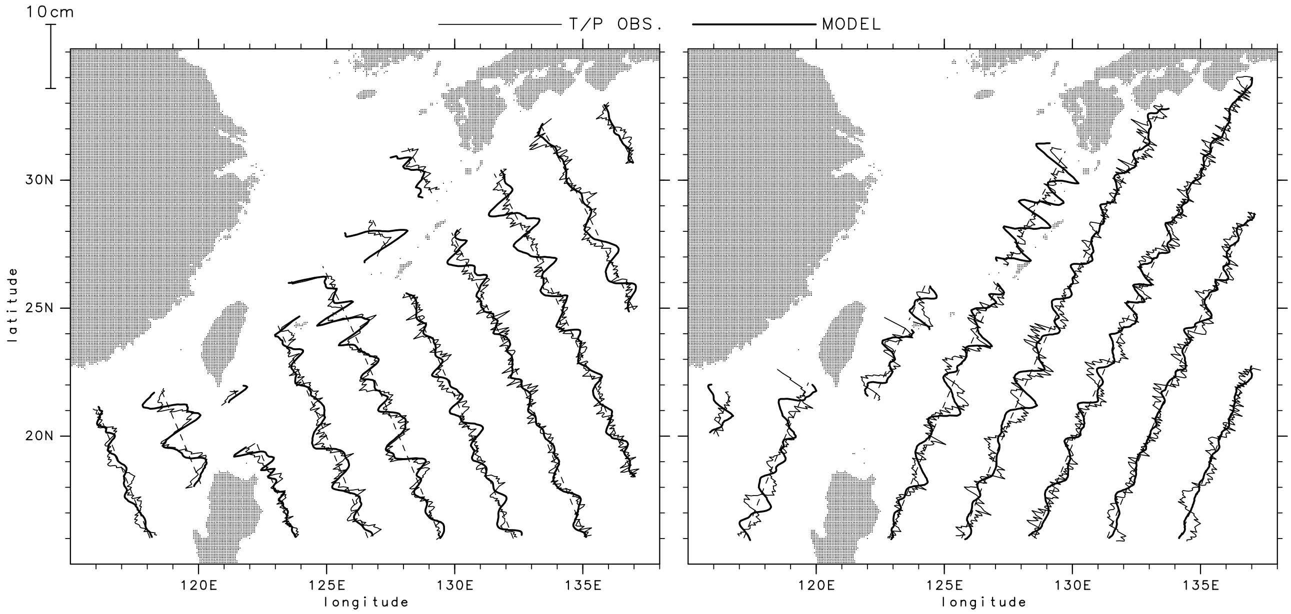


**Figure 10.** High-pass filtered amplitude of the $M_2$ tidal surface elevation along TOPEX/Poseidon (left) descending and (right) ascending ground tracks obtained from the model prediction (thick lines) and TOPEX/Poseidon altimeter observations (thin lines).

inhibited. Another reason is that shoreward propagating internal waves are strongly dissipated immediately after impinging onto the continental shelf by bottom friction.

[27] The integrated $M_2$ baroclinic energy flux across each section is shown by the blue numbers and arrows in Figure 12. The net $M_2$ baroclinic energy flux away from the Bashi/Luzon Strait amounts to 7.4 GW, 3.2 GW of which is directed toward the Pacific Ocean with the remaining 4.2 GW directed to the South China Sea. In the East China Sea, the net baroclinic energy flux to the Pacific Ocean amounts to 3.1 GW. It should be noted here that the integrated baroclinic energy flux is much less than the net baroclinic energy conversion estimated over the prominent topographic features, indicating that considerable fraction of the excited baroclinic energy is dissipated before radiating away from each area. Figure 12 also shows the predicted baroclinic energy flux for the run where the additional linear damping was assumed to vanish. Although the net baroclinic energy flux away from each area is somewhat increased in this case, it is still much less than the net baroclinic energy conversion over prominent topographic features within each area. This suggests that some mechanism other than our added linear damping is working to dissipate the excited baroclinic energy.

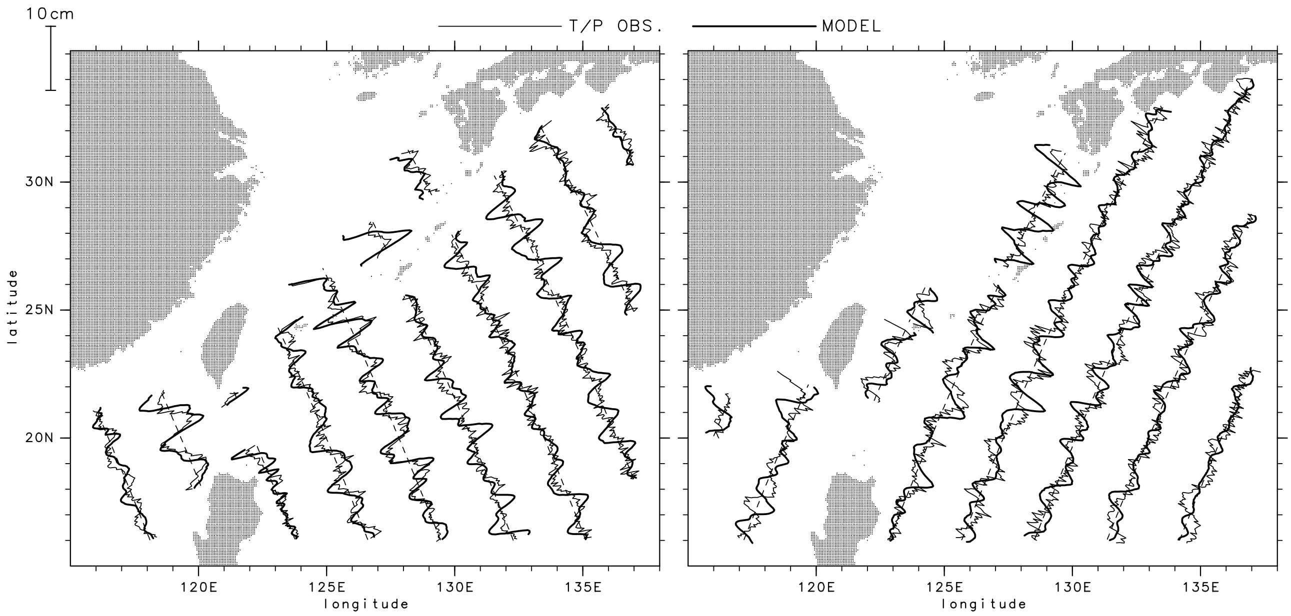


**Figure 11.** As in Figure 10 but for the run where the artificial linear damping of the $M_2$ internal tide completely omitted.

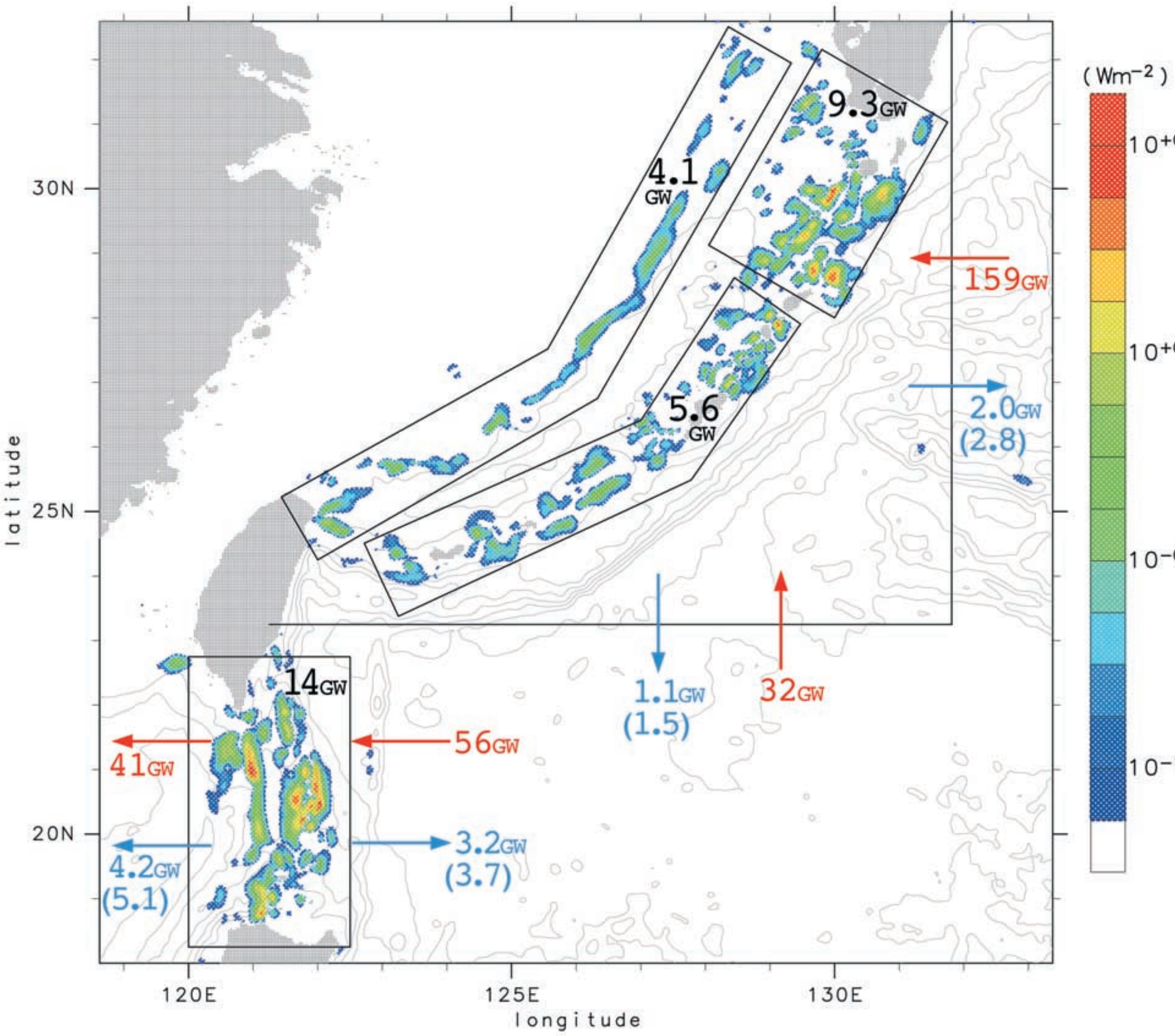


**Figure 12.** Model-predicted distribution of the depth-integrated conversion rate from the $M_2$ barotropic to baroclinic tidal energy (shown by the color shading). The background contours show the bathymetry (contour interval is 1000 m). The black numbers indicate the conversion rate integrated over the area including each prominent topographic feature. The red numbers and arrows indicate the value and direction of the $M_2$ barotropic energy flux across each section, whereas the blue numbers and arrows indicate the value and direction of the $M_2$ baroclinic energy flux across each section. The parenthesized blue numbers are the $M_2$ baroclinic energy flux estimates with the artificial linear damping of the $M_2$ internal tide completely omitted. For the details, see text.

[28] Assuming that advection of baroclinic energy is negligible in equation (8), the depth-integrated dissipation rate of the baroclinic energy averaged over one tidal period can be expressed as

$$\langle \overline{DIS_{bc}} \rangle \approx -\langle g\overline{\rho' w_{bt}} D \rangle + \left( \frac{\partial \langle \overline{P'U'}D \rangle}{\partial x} + \frac{\partial \langle \overline{P'V'}D \rangle}{\partial y} \right). \quad (13)$$

In order to quantify the distribution of baroclinic energy dissipation within the Bashi/Luzon Strait, the spatial distributions of the three terms in equation (13), namely, (a) the baroclinic energy conversion, (b) the baroclinic energy flux divergence, and (c) the difference between (a) and (b) are shown in Figure 14. Note that the artificial linear damping was assumed to vanish in Figure 14. Significant difference between the baroclinic energy conversion rate and the baroclinic energy flux divergence can be found at the location of strong baroclinic energy conversion. This indicates that internal tides are subject to strong local dissipation in proximity to their generation sites. The local dissipation within the Bashi/Luzon Strait amounts to 5.2 GW corresponding to about 40% of the baroclinic energy generated in this region. The same analysis indicates that there is an $M_2$ baroclinic energy dissipation rate of 5.9 GW in the Tokara Strait, 3.6 GW in the Ryukyu Island chain, and 3.5 GW over the continental shelf in the East China Sea, respectively. It follows that

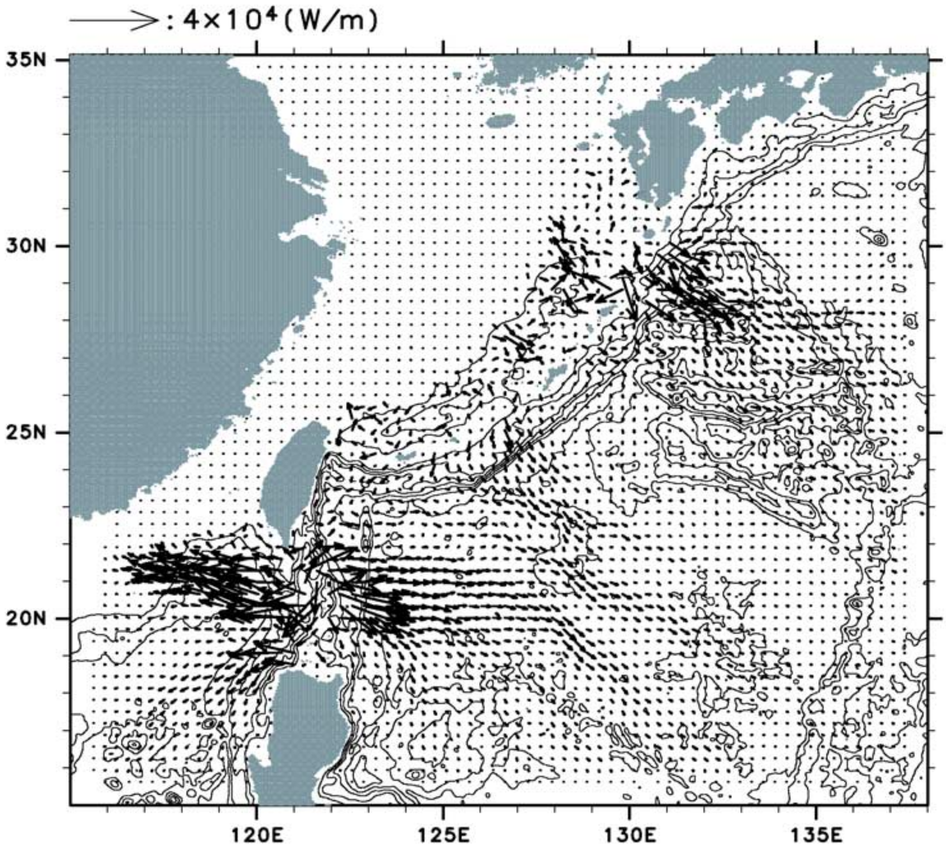


**Figure 13.** Model-predicted distribution of the depth-integrated $M_2$ baroclinic energy flux. The background contours show the bathymetry (contour interval is 1000 m).

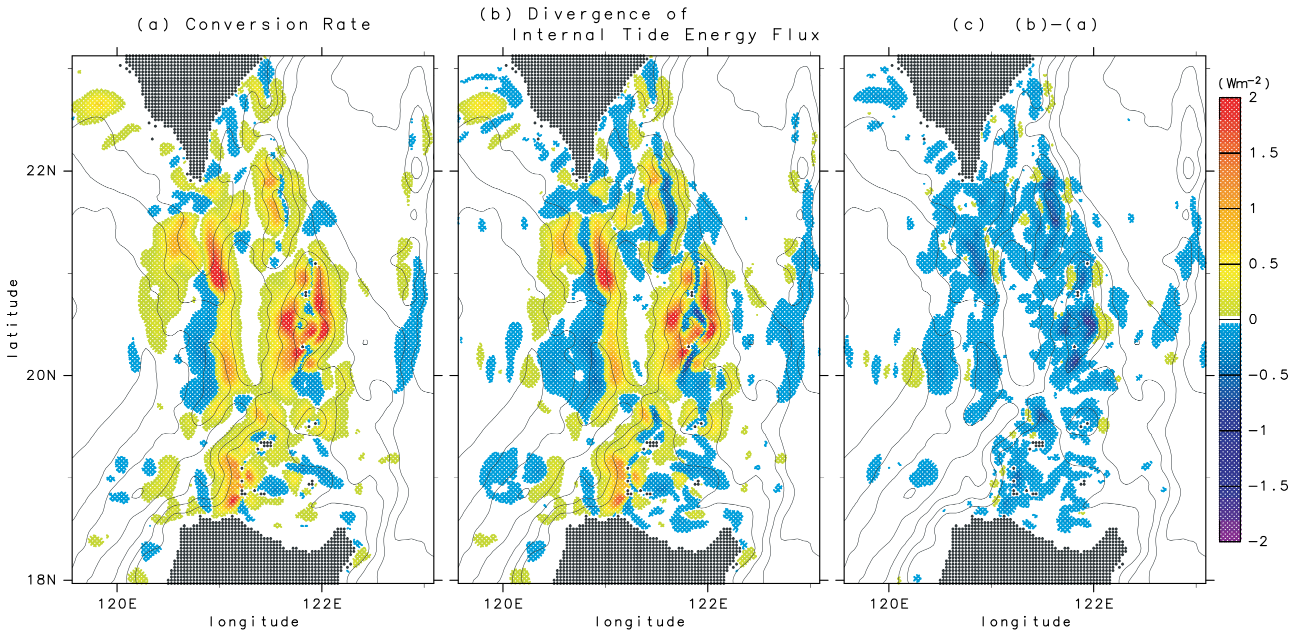


**Figure 14.** Model predicted distribution of (a) the depth-integrated conversion rate from the $M_2$ barotropic to baroclinic tidal energy, (b) the divergence of the depth-integrated $M_2$ baroclinic energy flux, and (c) the difference between them (the baroclinic energy flux divergence minus the baroclinic conversion rate) in the Bashi/Luzon Strait (shown by the color shading). The background contours show the bathymetry (contour interval is 1000 m). Note that the artificial linear damping of the $M_2$ internal tide was completely omitted.

**Table A1.** Summary of the Sensitivity Experiments in Appendix A

| Exp. | Horizontal Grid Size, deg | Vertical LevelNumber | Topography Averaging Radius, km | Comments | Baroclinic Conversion Rate [GW] (Relative Increase From Exp. A) | Baroclinic Energy Flux [GW] (Relative Increase From Exp. A) | Baroclinic Dissipation Rate [GW] (Relative Increase From Exp. A) |
|---|---|---|---|---|---|---|---|
| A | 1/32 | 50 | 10 | reference case | 14.9 | 9.0 | 5.9 |
| B1 | 1/16 | 50 | 10 | | 13.8 (−7%) | 8.3 (−8%) | 5.5 (−7%) |
| B2 | 1/64 | 50 | 10 | | 15.2 (+2%) | 9.4 (+4%) | 5.8 (−2%) |
| B3 | 1/32 | 100 | 10 | | 14.9 (+0%) | 8.9 (−1%) | 6.0 (+2%) |
| C1 | 1/32 | 50 | 5 | | 15.0 (+1%) | 8.4 (−7%) | 6.6 (+12%) |
| C2 | 1/32 | 50 | 7 | | 14.9 (+0%) | 8.6 (−4%) | 6.3 (+7%) |
| C3 | 1/32 | 50 | 14 | | 13.6 (−9%) | 8.5 (−6%) | 5.1 (−14%) |
| C4 | 1/32 | 50 | 20 | | 8.9 (−40%) | 6.1 (−32%) | 2.8 (−53%) |
| D1 | 1/32 | 50 | 10 | viscosity and diffusivity = 5 × (Exp. A) | 14.5 (−3%) | 7.4 (−18%) | 7.1 (+20%) |
| D2 | 1/32 | 50 | 10 | bottom drag coeff. = 5 × (Exp. A) | 14.5 (−3%) | 8.7 (−3%) | 5.8 (−2%) |

about 55% of the $M_2$ baroclinic energy generated in the whole analyzed model region is dissipated in close proximity to the baroclinic $M_2$ generation sites.

## 4. Summary and Discussion

[29] It is widely recognized that the internal tides play an important role by providing energy for deep ocean mixing. In the present study, the distribution and energetics of the $M_2$ internal tides generated in the East China Sea and adjacent seas have been numerically examined using a three-dimensional, primitive equation model that takes into account realistic tidal forcing as well as realistic bathymetry. The numerical experiment has shown that $M_2$ internal tides are effectively generated over prominent topographic features such as the subsurface ridges in the Bashi/Luzon Strait, the ridges along the Ryukyu Island chain and the continental shelf slopes in the East China Sea. The most energetic $M_2$ internal tides have been found in the Bashi/Luzon Strait and the Tokara Strait. These topographic features are all characterized by steep slopes at the depth of the thermocline. The $M_2$ surface tide is almost normally incident to these topographic features so that large amplitude internal tides are generated.

[30] The low vertical modes $M_2$ internal tides propagating away from these multiple source regions have been found to interfere with each other to create a complicated wave pattern in the western North Pacific. It has been found that the associated sea surface signatures observed by TOPEX/Poseidon altimeter are well reproduced by the numerical model so long as the dissipation of the propagating $M_2$ internal tide is adequately parameterized.

[31] *Hibiya et al.* [2002] numerically examined the nonlinear cascade of low vertical mode $M_2$ internal tide energy across the background GM internal wave spectrum down to dissipation scales. They showed that this energy cascade is dominated by parametric subharmonic instability (PSI) which is expected to occur only equatorward of 30°N, suggesting that baroclinic dissipation is dependent on latitudes. This is consistent with TOPEX/Poseidon altimeter data showing that the $M_2$ internal tide emanated from the Aleutian Ridge (~50°N) propagates much longer distance than the $M_2$ internal tide emanated from the Hawaiian Ridge (~25°N) [*Ray and Cartwright*, 1998].

[32] The rate of conversion of the $M_2$ barotropic to baroclinic tidal energy integrated over the whole analyzed model domain has been estimated to be 35 GW. We have found that roughly 10% of the energy in the $M_2$ surface tide incident on prominent topographic features is converted to $M_2$ internal tidal energy, nearly half of which is dissipated in close proximity to the generation sites. Strong local baroclinic dissipation was also pointed out over the Hawaiian Ridge where the baroclinic energy conversion reaches 20 GW, but the radiating baroclinic energy flux is only 9 GW [*Merrifield and Holloway*, 2002].

[33] The calculations in Appendix A indicate that compared to the baroclinic conversion rate, the predicted baroclinic dissipation rate is more dependent on the resolution of the bottom topography. This suggests that the local baroclinic dissipation is caused by shear and/or advective instability of small-scale internal waves generated and/or scattered at the bottom topography. Nevertheless, the detailed mechanism for this strong local dissipation must await future investigation.

## Appendix A: Sensitivity of Internal Tide Simulation to Various Parameters

[34] In order to examine the sensitivity of the calculated results to (1) the model grid spacing, (2) the spatial resolution of the bottom topography, and (3) the dissipation parameters, a set of numerical experiments were carried out for a localized area around the Bashi/Luzon Strait (see Figure 1). For each experiment, we calculate the $M_2$ baroclinic conversion rate and the divergence of the $M_2$ baroclinic energy flux both integrated over the model domain together with the difference between them, that is, the dissipation rate of the $M_2$ baroclinic energy (see equation (13)) within the model domain. Throughout the sensitivity experiments, we neglect the artificial linear damping for the $M_2$ internal tide. The summary of the sensitivity experiments is listed in Table A1.

[35] Experiment A is the reference experiment where the model parameters were the same as already discussed in the main part of the present paper. This run used a horizontal grid spacing of 1/32° with 50 evenly spaced vertical levels. The model's bottom topography was constructed by averaging the bathymetric data within a 10 km radius at each grid point.

[36] The sensitivity to the model grid spacing was examined through Experiments B1, B2, and B3. We can see that even when the horizontal grid resolution is halved (Exper-

iment B1) or doubled (Experiment B2) and/or the vertical grid resolution is doubled (Experiment B3), the predicted baroclinic conversion rate and the baroclinic dissipation rate are not significantly affected.

[37] The sensitivity to the spatial resolution of the bottom topography was examined through Experiments C1, C2, C3, and C4 where the averaging radius used to construct the model topography was 5, 7, 14, and 20 km, respectively. As the averaging radius increases and hence the spatial resolution of the bottom topography decreases, the baroclinic conversion rate and the baroclinic dissipation rate both diminish. In particular, when the averaging radius is doubled, the baroclinic conversion rate and the baroclinic dissipation rate decrease by 40% and 52%, respectively (Experiment C4). In contrast, Experiments C1 and C2 show that as the averaging radius falls below 10 km, the baroclinic conversion rate becomes saturated (Experiments C1 and C2). Although we should bear in mind that the bathymetric data of *Smith and Sandwell* [1997] is itself a smoothing representation of the actual bottom, the modeled generation of the $M_2$ internal tide seems to be almost independent of topographic features with horizontal scales less than 10 km.

[38] The sensitivity to the dissipation parameters is examined through Experiments D1 and D2. In Experiment D1, all the viscosity and diffusivity coefficients were increased by a factor of 5. As a result, the baroclinic dissipation rate increases by 20%, although the baroclinic conversion rate decreases only by 3%. Experiment D2 shows that the baroclinic dissipation rate does not change appreciably when the bottom drag coefficient is increased five fold. This suggests that bottom friction plays only a minor role in dissipating the $M_2$ internal tide in the generation region.

[39] **Acknowledgments.** The authors thank K. Matsumoto for kindly providing TOPEX/Poseidon altimetric data. They also extend their gratitude to John Toole and two anonymous reviewers for their invaluable comments and suggestions on the original manuscript.

## References

Baines, P. G. (1982), On internal tide generation models, *Deep Sea Res.*, *29*, 307–338.

Blumberg, A. F., and G. L. Mellor (1987), A description of a three-dimensional coastal ocean circulation model, in *Three-Dimensional Coastal Ocean Models*, *Coastal and Estuarine Stud.*, vol. 4, edited by N. Heaps, pp. 1–16, AGU, Washington D. C.

Egbert, G. D., and R. D. Ray (2000), Significant dissipation of tidal energy in the deep ocean inferred from satellite altimeter data, *Nature*, *405*, 775–778.

Hasumi, H., and N. Suginohara (1999), Effects of locally enhanced vertical diffusivity over rough bathymetry on the world ocean circulation, *J. Geophys. Res.*, *104*, 23,367–23,374.

Hibiya, T., M. Nagasawa, and Y. Niwa (2002), Nonlinear energy transfer within the oceanic internal wave spectrum at mid and high latitudes, *J. Geophys. Res.*, *107*(C11), 3207, doi:10.1029/2001JC001210.

Hsu, M. K., A. K. Liu, and C. Liu (2000), A study of internal waves in the China Seas and Yellow Sea using SAR, *Cont. Shelf. Res.*, *20*, 389–410.

Jayne, S. R., and L. C. St. Laurent (2001), Parameterizing tidal dissipation over rough topography, *Geophys. Res. Lett.*, *28*, 811–814.

Kang, S. K., S.-R. Lee, and H.-J. Lie (1998), Fine grid tidal modeling of the Yellow and East China Seas, *Cont. Shelf Res.*, *18*, 739–772.

Kantha, L. H. (1995), Barotropic tides in the global oceans from a nonlinear tidal model assimilating altimetric tides: 1. Model description and results, *J. Geophys. Res.*, *100*, 25,283–25,308.

Ledwell, J. R., E. T. Montgomery, K. L. Polzin, L. C. St. Laurent, R. W. Schmitt, and J. M. Toole (2000), Evidence for enhanced mixing over rough topography in the abyssal ocean, *Nature*, *403*, 179–182.

Lefévre, F., C. Le Provst, and F. H. Lyard (2000), How can we improve a global ocean tide model at a regional scale? A test on the Yellow Sea and the East China Sea, *J. Geophys. Res.*, *105*, 8707–8725.

Levitus, S., and T. P. Boyer (1994), *World Ocean Atlas 1994*, vol. 4, *Temperature, NOAA Atlas NESDIS 4*, Natl. Oceanic and Atmos. Admin., Silver Spring, Md.

Levitus, S., R. Burgett, and T. P. Boyer (1994), *World Ocean Atlas 1994*, vol. 3, *Salinity, NOAA Atlas NESDIS 3*, Natl. Oceanic and Atmos. Admin., Silver Spring, Md.

Lien, R.-C., and M. C. Gregg (2001), Observation of turbulence in a tidal beam and across a coastal ridge, *J. Geophys. Res.*, *106*, 4575–4591.

Matsumoto, K., T. Takanezawa, and M. Ooe (2000), Ocean tide models developed by assimilating TOPEX/Poseidon altimeter data into hydrodynamical model: A global model and a regional model around Japan, *J. Oceanogr.*, *56*, 567–581.

Matsuno, T., S. Kanari, C. Kobayashi, and T. Hibiya (1994), Vertical mixing in the bottom mixed layer near the continental shelf break in the East China Sea, *J. Oceanogr.*, *50*, 437–448.

Matsuno, T., T. Hibiya, S. Kanari, and C. Kobayashi (1997), Small scale internal waves and turbulent fluctuations near the continental shelf break in the East China Sea, *J. Oceanogr.*, *53*, 259–269.

McComas, C. H., and P. Müller (1981), The dynamic balance of internal waves, *J. Phys. Oceanogr.*, *11*, 970–986.

Mellor, G. L., and T. Yamada (1982), Development of a turbulent closure model for geophysical fluid problems, *Rev. Geophys.*, *20*, 851–875.

Merrifield, M. A., and P. E. Holloway (2002), Model estimates of $M_2$ internal tide energetics at the Hawaii Ridge, *J. Geophys. Res.*, *107*(C8), 3179, doi:10.1029/2001JC000996.

Munk, W. H. (1997), Once again: Once again-tidal friction, *Prog. Oceanogr.*, *40*, 7–35.

Munk, W. H., and C. Wunsch (1998), Abyssal recipes II: Energetics of tidal and wind mixing, *Deep Sea Res., Part I*, *45*, 1977–2010.

Niwa, Y., and T. Hibiya (2001), Numerical study of the spatial distribution of the $M_2$ internal tide in the Pacific Ocean, *J. Geophys. Res.*, *106*, 22,441–22,449.

Polzin, K. L., J. M. Toole, J. R. Ledwell, and R. W. Schmitt (1997), Spatial variability of turbulent mixing in the abyssal ocean, *Science*, *276*, 93–96.

Ray, R. D. (2001), Estimates of internal tide energy fluxes from TOPEX/Poseidon altimetry: Central North Pacific, *Geophys. Res. Lett.*, *28*, 1259–1262.

Ray, R. D., and D. E. Cartwright (1998), Ocean self-attraction and loading in numerical tidal models, *Mar. Geod.*, *21*, 181–192.

Ray, R. D., and G. T. Mitchum (1996), Surface manifestation of internal tides generated near Hawaii, *Geophys. Res. Lett.*, *23*, 2101–2104.

Smagorinsky, J. S. (1963), General circulation experiments with the primitive equations: I. The basic experiment, *Mon. Weather Rev.*, *91*, 99–164.

Smith, W. H. F., and D. T. Sandwell (1997), Global sea floor topography from satellite altimetry and ship depth soundings, *Science*, *277*, 1956–1962.

T. Hibiya and Y. Niwa, Department of Earth and Planetary Science, Graduate School of Science, University of Tokyo, Tokyo 113-0033, Japan. (hibiya@eps.s.u-tokyo.ac.jp; niwa@eps.s.u-tokyo.ac.jp)